Rapid formation of large aggregates during the spring bloom of Kerguelen Island: observations and model comparisons.

Marie-Paule Jouandet
Mediterranean Institute of Oceanography (MIO)
Unité mixte : Aix Marseille Université - CNRS – IRD
13288 Marseille Cedex 09, France
Email: **marie-paule.jouandet@univ-amu.fr**

George A. Jackson
Department of Oceanography
Texas A&M University
College Station, TX 77845-3146, USA
Email: **gjackson@tamu.edu**

François Carlotti
Mediterranean Institute of Oceanography (MIO)
Unité mixte : Aix Marseille Université - CNRS – IRD
13288 Marseille Cedex 09, France
Email: **francois.carlotti@univ-amu.fr**

Marc Picheral
CNRS, UMR 7093, LOV, Observatoire océanologique
F-06230, Villefranche/mer, France
Email: **picheral@obs-vlfr.fr**

Lars Stemmann
Sorbonne Universités, UPMC Univ Paris 06, UMR 7093, LOV, Observatoire océanologique,
F-06230, Villefranche/mer, France
Email: stemmann@obs-vlfr.fr

Stéphane Blain
[1]Sorbonne Universités, UPMC Univ Paris 06, UMR 7621, Laboratoire d'Océanographie Microbienne, Observatoire Océanologique, F-66650 Banyuls/mer, France

[2] CNRS, UMR 7621, Laboratoire d'Océanographie Microbienne, Observatoire Océanologique, F-66650 Banyuls/mer, France
Email : stephane.blain@obs-banyuls.fr

Abstract

While production of aggregates and their subsequent sinking is know to be one pathway for the downward movement of organic matter from the euphotic zone, the rapid transition from non-aggregated to aggregated particles has not been reported previously. We made one vertical profile of particle size distributions (PSD, sizes ranging from 0.052 to several mm in equivalent spherical diameter) at pre-bloom stage and seven vertical profiles three weeks later over a 48 h period at early bloom stage using the Underwater Vision Profiler during the Kerguelen Ocean and Plateau Compared Study cruise 2 (KEOPS 2, October–November 2011). In these natural iron-fertilized waters southeast of Kerguelen Island (Southern Ocean), the total particle numerical abundance increased by more than 4 fold within this time period. A massive total volume increase associated with particle size distribution changes was observed over the 48 h survey, showing the rapid formation of large particles and their accumulation at the base of the mixed layer. The results of a one dimensional particle dynamics model support coagulation as the mechanism responsible for the rapid aggregate formation and the development of the V_T subsurface maxima. The comparison of V_T profiles between early bloom stage and pre-bloom stage points out an increase of particulate export below 200 m when bloom has developed. These results highlight the role of coagulation to form large particles and to trigger carbon export at early stage of a natural iron fertilized bloom, while zooplankton grazing may dominate later in the season. The rapid changes observed points out the critical need to measure carbon export flux with high sampling temporal resolution. Our results are the first published in situ observations of the rapid accumulation of marine aggregates and their export and the general agreement of this rapid event with a model of phytoplankton growth and coagulation.

1 Introduction

Biological particle production and sedimentation out of the euphotic layer to underlying waters is the major mechanisms for atmospheric CO_2 removal and the redistribution of carbon and associated nutrients in the ocean. The fate of this exported particulate carbon is a function of the plankton community producing them in the upper layer and particle transformation by microbes and zooplankton during their descent to the deep sea. Physical aggregation of particles is one key process in this transformation and transport and can explain the rapid formation and export of large particles during bloom conditions.

The Southern Ocean is the largest High Nutrients Low Chlorophyll (HNLC) region of the global ocean. However, several areas in this biological desert display strong seasonal phytoplankton blooms. Since the HNLC regions result from low supplies of the crucial nutrient iron, the hypothesis is that these blooms are supported by natural sources of iron, most likely supplied from local islands and shallow sediment (Moore and Abbott, 2002; Tyrrell et al., 2005; Blain et al., 2007; Pollard et al., 2007).

The impact of iron on the biological carbon pump has been investigated in these natural bloom regions (Blain et al., 2007; Pollard et al., 2007) and in patches formed by adding iron to localized HNLC regions (Boyd et al., 2000, 2004; Gervais et al., 2002; Buesseler et al., 2004, 2005; de Baar et al., 2005; Hoffmann et al., 2006; Smetacek et al., 2012; Martin et al., 2013). The observations made during the natural iron fertilization programs KEOPS1 and CROZEX (CROZet natural iron bloom and EXport experiment) documented a two-fold greater carbon export flux downward from the mixed layer (ML) in the natural iron fertilized bloom relative to that in unfertilized surrounding waters (Jouandet et al., 2008, 2011; Savoye et al., 2008; Pollard et al., 2009). An increase in POC flux after artificial fertilization experiments was detected only during SOFex (Southern Ocean Fe Experiment, Buesseler et al., 2005) and EIFEX (European Iron Fertilization Experiment, Smetacek et al., 2012).

Optical examination of particles trapped in polyacrylamide gels during KEOPS1 found that export at 100-430 m was dominated by fecal pellets and fecal aggregates (Ebersbach and Trull, 2008) which can be considered as a form of indirect export. (Note that we consider direct export to be the flux of phytoplankton cells, either alone or in aggregates). By contrast, the CROZEX experiment observed direct export of surface production by a diverse range of diatoms (Salter et al., 2007), consistent with phytoplankton aggregation enhancing particulate

flux. The lack of phytoplankton aggregation due to insufficient biomass has been invoked as the reason for which carbon export flux in SOIREE (Southern Ocean Iron Release Experiment) were not enhanced (Waite and Nodder, 2001; Jackson et al., 2005). The different results for these systems reflect differences in physical forcing factors, experimental duration, and seasonal evolution of the biological community.

Because of the complexity of the export system, there are still extensive unknowns about the effect of iron fertilization on carbon export from the surface to the bottom layer. The aim of our study is to investigate processes responsible for the formation of large particles (> 52 μm) at a short time scale during bloom development in the surface ML.

We combine multiple vertical profiles of large particles size spectra collected over a relatively short period during KEOPS2 with a one dimensional particle dynamics model that incorporates phytoplankton growth as a function of light and nitrate concentration and coagulation as function of aggregate size. We measured particle distributions using the Underwater Vision Profiler (UVP) deployed at a bloom station above the Kerguelen plateau under pre-bloom conditions and at an early bloom stage during a period of rapid change. The coagulation model used here is an extension of a zero-dimensional model that simulates abundances of phytoplankton cells in the surface mixed layer as well as the size distributions of settling particles (e.g., Jackson et al., 2005; Jackson and Kiørboe, 2008). Here it has been extended into a one-dimensional model to describe the vertical distribution of phytoplankton in the mixed layer and the formation, distribution, and flux of aggregates. The comparison between observed and modelled particle size distribution provides a unique opportunity to test the usefulness of the coagulation theory to explain rapid formation of large aggregates during the early stage of a phytoplankton bloom.

2 Material and methods

2.1 Field measurements

The station A3 (50°380 S, 72°050 E), located above the Kerguelen plateau, is characterized by a weak current (speed< 3 cm s^{-1}, Park et al., 2008b), which results in a water mass residence time of several months. This long residence time allows the bloom to develop and persist over an entire season in response to natural iron fertilization (Blain et al., 2007).

During KEOPS2, Station A3 was sampled first during pre-bloom conditions on 21 October 2011 (A3-1) and was revisited during the early bloom from 15 to 17 November (A3-2), 2 weeks after the bloom had started. High sampling frequency started during the second visit at midnight on 15 November (Table 1).

The Underwater Vision Profiler 5 (UVP 5 Sn002) used in the present study was a component of the rosette profiler system. The UVP5 detects and measures particles larger than 52 μm on images acquired at high frequency (Picheral et al., 2010). Images were taken and data recorded at a frequency of 6Hz, corresponding to a distance of 20 cm between images at the 1 m s^{-1} lowering speed of the CTD. The observed volume per image is 0.48 dm^3; the total volume sampled for the 500 m depth profiles at Station A3 was 1.2 m^3. The instrument takes a digital picture of a calibrated volume lit from the side. The image is scanned for particles and particle dimensions are measured. The pixel area (S_p) for each object is converted to cross-sectional area (S_m) using the calibration equation $S_m = 0.00018\ S_p^{1.452}$. An equivalent spherical diameter d is calculated for that cross-sectional area. Hydrographic and biogeochemical properties, including density, fluorescence, turbidity (as determined by a transmissometer using a wavelength of 660nm and a 25 cm path length), were measured simultaneously with a conductivity-temperature-depth system (Seabird SBE-911+CTD) linked to a Seapoint Chelsea Aquatracka III (6000 m) chlorophyll fluorometer and a WET Labs C-Star (6000 m) Transmissiometer.

We also present selected results of chlorophyll *a* (Chl *a*) and nitrate concentrations, as well as relative biomass of different phytoplankton size classes. Chl *a* and pigment concentrations were measured using high performance liquid chromatography (HPLC) following the method described in Lasbleiz et al. (2014); the fraction of a phytoplankton group relative to the total biomass was calculated using the model of Uitz et al. (2006). Nitrate was analysed with a Technicon autoanalyzer as described in Tréguer and Le Corre (1975).

2.2 Data processing

The particles in each 5 m depth interval, with depth determined from the associated CTD measurements, were sorted into 27 diameter intervals (from 0.052 to 27 mm, spaced geometrically), and concentrations calculated for each diameter and depth interval. We further analysed size spectra having a minimum of 5 particles per size bin and depth interval; this criterion eliminated bins with $d > 1.6$ mm. The depth distributions of particles are

summarized in terms of their total number N_T (# L^{-1}) and volume V_T (mm^3 L^{-1} = ppm) concentrations.

Particle number distributions (n) were calculated by dividing the number of particles (ΔN) within a given bin by the width of the ESD bin (Δd) and the sample volume. The resulting units are # cm^{-4}. The distributions are usually plotted in a loglog plot because of the large ranges in n and d. To compensate for these ranges, the results are often displayed as nVd spectra, where n is multiplied by the median diameter (d) and the spherical volume $V = \pi/6\ d^3$ for the particle size range. This form of the particle size distribution has the advantage that the area under the curve is proportional to the total particle volume concentration when nVd is plotted against log(d). The carbon export flux F_{POC} (mg C m^{-2} d^{-1}) can be estimated from the size spectra using the empirical relationship:

$$F_{POC} = Ad^b \quad (1)$$

where d is the diameter in mm, A = 12.5 and b = 3.81 (Guidi et al., 2008). Guidi et al. (2008) developed the relationship by comparing particle size spectra to sediment trap collection rates at locations around the world. The value of b is less than the value of 5 expected for spherical particles of constant density (for which mass increases as d^3, and sinking speed as d^2). It is consistent with marine aggregates having increasing porosity with increasing size (e.g., Alldredge and Gotschalk, 1988).

2.3 Model equations and parameterization

The biological model describes the growth rate of phytoplankton in the water column as a function of light and nutrient (nitrate) concentration. The model uses a maximum phytoplankton specific growth rate G_{max}= 0.45 d^{-1} (Timmermans et al., 2004; Assmy et al., 2007). Phytoplankton cells are transformed into aggregates by differential settling and shear using the standard coagulation model of Jackson (1995). Aggregates are also fragmented in two similar parts using size-dependent disaggregation rates (Jackson, 1995). The primary phytoplankton cells are chosen to match the size of *Fragiliaropsis kerguelensis* which was the dominant species under pre-bloom conditions (Armand, Pers. Com.). A single phytoplankton cell has d_1 =20 μm, a density 1.0637 g cm^{-1}, and a resulting settling speed v_1 = 1.05 m d^{-1}. The probability that two particles colliding stick together, α, is assumed to be 1. The average

turbulent shear rate is $\gamma = 1\ s^{-1}$ (Jackson et al., 2005). The initial abundance of phytoplankton is 10 cells cm^{-3}. These and other parameter values are shown in Table 2. The one-dimensional model simulates the distribution of particles of different sizes, including solitary phytoplankton cells, and nitrate concentrations at 2 m depth intervals within the 0–150 m layer. This depth range corresponds to the average surface ML thickness during the survey (Table 1). Neither zooplankton grazing nor particle transformation by bacterial processes is included in these simulations. The model is described in greater detail in Appendix A.

While the concept of spherical diameter is simple for a solid sphere, it is not for irregular marine aggregates, with different shapes, assembled from multiple sources, having water in the interstices between their components and yielding different sizes for different measurement techniques (e.g., Jackson, 1995). The simplest diameter is the conserved diameter d_c, the diameter if all the solid matter was compressed into a solid sphere. It has the advantage that when two particles collide and form a new particle, the conserved volume of the new particle is the sum of the conserved volumes of the two colliding particles. The particle diameter d determined by the UVP is larger than d_c because aggregate size is determined from the outer shape of the aggregate and thus contains pore water between source particles. The relationship between the two measures of particle diameter is described using the fractal dimension (see Appendix A). The model calculations use d_c. However, all model results shown here use the apparent diameter d_a, which is used to approximate the diameter reported by the UVP. The value of d_a is calculated from dc using the fractal relationship and a fractal dimension of 2 (Appendix A). Note that reported values of the fractal dimension vary widely, from 1.3–2.3 (Burd and Jackson, 2009). The value of 2 used here is in this range and yields peaks in the nVd distributions similar to those determined from UVP measurements, unlike values of 2.1 and 1.9 (not shown).

3 Results

3.1 Observations

3.1.1 Biogeochemical and physical context

The water column was characterized by a deep mixed layer (~150 m) during the pre-bloom and early bloom surveys, with a range of 120 to 171 m (Figs. 1 and 2). Isopycnal

displacements of up to 50 m can be seen in the density profiles. Such vertical movements are known to result from semi-diurnal internal tides in this region (Park et al., 2008a). The fluorescence and Chl *a* concentrations show a 4-fold increase from A3-1 (21 October) to A3-2 (15–17 November), with Chl *a* concentrations at the surface increasing from 0.5 to ~2 μg L^{-1} (Figs. 1 and 2). The Chl *a* profile determined using bottle samples for station A3-2 was characterized by a subsurface maximum at 170 m, at the bottom of the mixed layer (Fig. 3). The chlorophyll profiles determined using the in situ fluorometer were either relatively constant or had maxima at 50 m or shallower (Figs. 1 and 2). Variations in the maximum depth of fluorescence from the in situ profiles were associated with temporary deepening of the mixed layer at 7.50 AM and 7.15 PM on 16 November and at 5.30 AM on 17 November. In the surface mixed layer, the beam attenuation coefficient (turbidity) had a similar distribution as fluorescence (Figs. 1 and 2). The two were, in fact, highly correlated in the surface mixed layer (r = 0.95), which was not always the case in deeper layers. Nitrate concentrations at A3-1 were 28 to 30 μM in the mixed layer, and then decreased by 4 μM at A3-2 (Fig. 3a). Pigment analysis (Fig. 3) and cell counts of phytoplankton captured in nets (Armand., Pers. Com.) showed that the phytoplankton community was dominated by diatoms, *Fragilariopsis* at A3-1 and an assemblage of *Fragilariopsis*, *Chaetoceros* and *Pseudonitschia* at A3-2. The zooplankton community was dominated by copepods with a mixture of adult (50.5 %) and copepodites stage (49.5 %) at A3-2 (Carlotti et al., 2014). Zooplankton biomass increased from 1.4 gC m^{-2} at A3-1 to 4.1 gC m^{-2} at A3-2 over the 0–250 m layer, and was thus more than 2 fold lower than the mean biomass of 10.6 gC m^{-2} measured at A3 in summer during KEOPS1 (Carlotti et al., 2008).

3.1.2 Evolution of the total abundance and volume distributions in the mixed layer

In the pre-bloom profile, total particle abundance (N_T) and volume (V_T) distributions at station A3 were characterized by a two layer structure (Fig. 1B). The shallower layer had relatively uniform N_T (V_T) values of 90 ± 5 particles L^{-1} (0.3±0.1 mm^3 L^{-1}) between 0 and 100 m*;* the second layer, from 100 m to the base of the ML (166 m), had subsurface N_T and V_T maxima of 142 particles L^{-1} and 0.45 mm^3 L^{-1}. There was a two-fold increase in N_T at the first cast of the early bloom (A3-2/1), with values reaching 200±7 # L^{-1} in the first hundred meters and a subsurface maximum of 300 # L^{-1} (Fig. 4). V_T also increased by one order of magnitude reaching a value of 3 mm^3 L^{-1} at the depth of the subsurface maxima (Fig. 4). In subsequent casts, there was a 40 m thick surface layer with constant N_T and V_T and a subsurface

maximum present at variable depths. Particularly striking was the rapid and continuous increase of both N_T and V_T from A3-2/1 to A3-2/5 over a roughly 24 h time period. This was more than a redistribution of aggregates, as N_T and V_T integrated over the ML increased from 282 to 743 # m^{-2} and from 101 x 10^3 to 1500 x 10^3 mm^3 m^{-2}. There was a further increase by the end of the survey in the maximum V_T to mm^3 L^{-1}, almost two orders of magnitude greater than for the pre-bloom situation.

3.1.3 Evolution of size distributions with depth and time during the early bloom phase

The particle size distributions (PSD) calculated from the UVP observations provide additional insight to the change in particle abundance during the 2 d spring observation period. In order to display the vertical structure of PSD, we compare the average over the nominal euphotic zone (0 to 40 m) to the average over the 40 m centred on the subsurface particle maximum. Particles larger than 129 μm were more abundant in the subsurface layer (Fig. 5A). Consistent with the analysis in the previous section, the smallest difference between the 2 layers occurred during the pre-bloom sampling (A3-1). The maximum increases were in the 0.128 - 0.162 mm and 0.204 - 0.257 mm size classes, with abundance increases of 66 # L^{-1} and 62 # L^{-1} for A3-2/3. The increase was also substantial in the 0.4-0.5 mm size range. The cumulative volume distribution in the 0-40 m euphotic zone shows that increased particle volumes resulted from formation of larger particles (Fig. 5b).

Within the vertical particle maxima, half of V_T was in particles with d > 0.5 mm at the start of the survey, while these larger particles provided more than 80% at the end. The largest change in size spectra was in the approximately 17.5 h period between morning (A3-2/2) and middle of the night (A3-2/5) of 16 November.

The *nVd* size distribution for profile A3-2/5 is shown in detail in Fig. 6. The area under the curve at a constant depth is proportional to the particle volume V_T at that depth. Between the surface and 60 m most particle volume is in the smallest size class with particles d ranging between 200 and 500 μm. Massive changes occurred with depth with an increase of the volume and d. The volumes from 60 m to 150 m are supported by larger particles ranging between 0.65 mm to 1.1 mm, with a peak of 30 ppm for a d of 1 mm.

3.1.4 Particle distributions below the ML

In the first 50 m below the ML, V_T values mirrored those in the overlying waters, increasing to 20 ppm by the end of the survey period (A3-2/7) (Fig. 7). V_T decreased from the base of the ML to 200 m by about a factor of 20 for A3-2/6 and A3-2/7. Below 200 m, the depth limit for winter mixing, there was no change in V_T during the two days survey. The average V_T was 0.40 ± 0.10 and 0.38 ± 0.10 mm^3 L^{-1} at 250 and 350 m. There was an increase in V_T at about 475 m caused by resuspension from the bottom, as documented during KEOPS1 (Chever et al., 2010; Jouandet et al., 2011). The particle number distribution (n) decreased from the base of the mixed layer to 350 m in all size classes, particularly for particles larger than 500 μm, which were no longer detectable (Fig. 7B).

3.1.5 Relationship between particle volume and fluorescence

As mentioned, there was no simple correlation between V_T and fluorescence. However, separating the observations by depth layers (the mixed layer, the base of the ML to 200 m and deeper than 200 m) reveals a pattern (Fig. 8). In the shallowest layer, there was an increase from the pre-bloom values of low fluorescence and particle volume for A3-1 (21 October) to high fluorescence and low particle volume for A3-2/1 (15 November, 11.20 PM). This is consistent with an increase in phytoplankton biomass but no aggregate production. For A3-2/2, there are hints of an increase of V_T, which became pronounced in subsequent casts. The increased particle concentrations were accompanied by a slight decrease in fluorescence. For the seven casts performed during the early bloom stage, the correlations between fluorescence and V_T were negative (-0.53), with a slope of -0.015 μg Chl mm^{-3}. In the second layer, immediately below the surface mixed layer, fluorescence and V_T increased together, with a positive correlation coefficient (0.68) and a slope of 0.036 μg Chl mm^{-3} (Fig. 8). This is consistent with no phytoplankton growth in this depth layer, but with phytoplankton and aggregates arriving together from above, presumably in aggregates. There was no correlation between fluorescence and V_T below 200 m during this period.

3.1.6 POC flux

The flux at 200 m computed from the UVP particle size distributions increased from 1.8 mg m^{-2} d^{-1} during pre-bloom conditions to 23 mg Cm^{-2} d^{-1} during the early bloom (last cast of the survey). This increase over time as estimated from UVP measurements was also evident at 400 m but with a smaller change, with F_{POC} increasing from 1.04 to 3.5 mg C m^{-2} d^{-1} at 400 m (Table 3).

Our POC flux estimates at 200 m for the spring bloom are in the range of the POC flux estimated from the sediment trap PPS3/3 (27±8 mg C m^{-2} d^{-1}) and below the estimates made from the gel trap (F_{POC} = 66 mg C m^{-2} d^{-1}) and from the thorium deficit ($F_{POC\text{-}Th}$ = 32 mg C m^{-2} d^{-1}) (Laurenceau et al., 2014; Planchon et al., 2014). $F_{POC\text{-}Th}$ at 100 m increased from pre-bloom to early bloom but stayed unchanged at 200 m. The $F_{POC\text{-}Th}$ at 200 m was estimated at A3-2/1, consistent with UVP observations that did not record any V_T increase.

3.2 Simulations

3.2.1 Development of the phytoplankton bloom

The phytoplankton in the model grew exponentially in the upper part of the water column for the first eight days of the simulation, slowing down as light limitation became important (Fig. 9A). The specific rate of integrated population growth (0 to 150 m) was ~0.06 d^{-1} for this initial period. The peak phytoplankton biomass was 2 μg Chl L^{-1} at about 10 m depth on day 13. The phytoplankton biomass decreased slightly when coagulation became an important removal mechanism by day 20, with surface phytoplankton biomass of 1.7 μg Chl L^{-1}, a maximum concentration of 1.9 μg Chl L^{-1} at 15 m, and a minimum concentration of 0.2 μg Chl L^{-1} at 150 m. Surface nitrate concentrations decreased from the initial 30 to 25 μM by day 20 (Fig. 9B).

3.2.2 Development of the aggregate volume

Aggregates with d_a > 100 μm appeared by day 14, when the total volume peaked at 1.3 ppm at 40 m (Fig. 9C). As the phytoplankton biomass increased, the maximum total volume also increased. The depth of the aggregate maximum deepened as the aggregates sank, becoming 17 ppm below 140 m on day 18. By day 20, the initial rapid coagulation phase ended, with the

maximum phytoplankton biomass decreasing slightly in the upper 50 m and the aggregates at the base of the mixed layer slowly decreasing. The vertical size distribution at day 20 provides further details on the system (Fig. 10). The nVd_a size distribution shows the distribution of particle volume, with the area under the curve being proportional to the particle volume when displayed with a logarithmic d_a axis, as here (Fig. 10). Most particle volume at the surface is in the smallest particles, the single phytoplankton cells. At 10 m depth, aggregates appear with a maximum nVd_a value at d_a = 200 μm. With increasing depth, the total volume and the diameter of the maximum nVd_a both increase. The d_a at the maximum became 0.9 mm at about 70 m depth, remaining constant with increasing depth, even though the total volume continued to increase with depth.

4 Discussion

4.1 Role of coagulation in the rapid changes observed

There are several striking correspondences between the observations at A3 during KEOPS2 and the one-dimensional coagulation model used here. First, the formation of large aggregates observed over the short timescale (<2 d) was mimicked by the model. The simulation results highlight the ability of coagulation to change the system state on short times that require a frequent sampling regime to observe. The shapes of the *nVd* spectra at the base of the mixed layer, centred at 0.9 mm for the model and 1 mm for the observations, with half widths of 1 mm for the model and 0.6 mm for A3-2/5 (Fig. 6, 10), were very similar. The transition to rapid coagulation took place when relatively little of the initial nitrate had been consumed in the model (4 μM), consistent with the 3.6 μM decrease observed from A3-1 to A3-2 (Fig. 3 & 9).

Coagulation theory has been used to predict the maximum phytoplankton biomass in the ocean (e.g., Jackson and Kiørboe, 2008). Coagulation of phytoplankton cells is a non-linear process. Rates increase dramatically as phytoplankton biomass increases, eventually removing cells as fast as they divide. The volume concentration at which this occurs is the critical volume concentration (Jackson, 2005):

$$V_{cr} = \pi\mu(8\alpha\gamma)^{-1} \quad (2)$$

For this calculation, we assumed an average specific growth rate for the population increase rate $\mu = 0.1$ d^{-1} , in agreement with measurements made by Closset et al. (this volume), α=1, and γ=1 s^{-1}. Note that the average increase rate is not the same as the peak rate G_{max}. For a POC: volume ratio of 0.17 g C cm^{-3} (Jackson and Kiørboe, 2008) and a carbon to chlorophyll ratio of 50 g C: g Chl, this is equivalent to 1.5 µg Chl a L^{-1}. This value for V_{cr} is remarkably close to the maximum concentrations of 2-2.2 µg Chl *a* L^{-1} observed during the particle formation at A3-2.

The rapid production of aggregates at station A3 observed in this study provides an impressive example of the importance of coagulation in controlling PSD and vertical export of primary production.

The nature of the exported material collected in a free drifting sediment gel trap at 210 m supports also the importance of algal coagulation in forming the exported material (Laurenceau et al., 2014). Their analysis shows that the particle flux number and volume were dominated by phytoaggregates over the 0.071-0.6 mm size range.

4.2 Limitations of the model

There are, not unexpectedly, differences between model results and observations. To start, fluorescence profiles are relatively constant through the surface mixed layer in the observations, but have a pronounced shallow subsurface chlorophyll maximum in the model because of the higher light levels near the surface. Increased mixing in the model could smooth the chlorophyll profiles, as well as the distribution of particle volume. Simulations made using a much larger mixing coefficient (1000 m^2 d^{-1}) yield a smaller difference in chlorophyll between the surface and 150 m, but there is still a difference of 0.8 µg Chl L^{-1} over the depth range (results not shown). The vertical mixing rate estimated for the iron fertilization experiment EIFEX, 29 m^2 d^{-1}, was actually smaller than that used in these simulations, 100 m^2 d^{-1} (Smetacek et al., 2012). A previous model of phytoplankton growth in the Keguelen region discussed large scale horizontal patterns but unfortunately did not display vertical distribution (Mongin et al., 2008). Whatever the reason for the relatively uniform fluorescence profile, it is not simply a faster diffusive mixing rate. Those differences illustrate the difficulty of building a realistic phytoplankton growth model in the region to drive the coagulation model. The shallower phytoplankton distribution does affect the distribution of aggregates as well.

In a model such as the one used in the present study, there are many parameters and modelled processes that influence the final results. These include parameters such as the fractal dimension, the size of the phytoplankton cells, or processes to describe diatom chains growth, disaggregation rates, and grazing. While the parameters could be tuned systematically to give an improved fit, what is striking is the similarity between observations and the model without such a systematic fitting procedure. One important parameter that was varied during model development to adjust the results was the fractal dimension. Decreasing it decreased the diameter of the peak value of *nVd*. The value that was chosen, D_{fr}=2, was similar to some of the estimates of fractal dimension noted above and did provide the correct *nVd* distribution when coagulation occurred.

Other processes are known to affect particle concentrations and fluxes, most notably physical process such as advection and biological processes such as zooplankton grazing and fecal pellet production (e.g., Lampitt et al., 1993; Stemmann et al., 2000; Turner et al., 2002). The importance of advection could be inferred from time series measurements of LADCP. The results indicated a current below 0.1 m s^{-1}, with negligible changes over the survey in the 0-200 m depth layer (Park, pers.com.). The abundance and volume of zooplankton larger than 0.7 mm, as well as fecal sticks/pellets and aggregates, were estimated from the identification of organism in the vignettes recorded by the UVP using the Zooprocess imaging software (see Picheral et al., 2010). The volume of copepods did not increase through the early bloom survey, suggesting that they were not responsible for the observed rapid increase in particles. Ingestion rates were also estimated from zooplankton biomass using the relationship detailed in Carlotti et al. (2008) using the biomass results integrated over the 0–250 m layer. The ingestion rate was 1.36 mg C d^{-1} during the early bloom cast and lower than during the KEOPS1 summer cruise. In addition, fecal pellet production should have a diurnal signal (Carlotti et al., 2014), which was not observed in the V_T profiles. Lastly, fast sinking fecal pellets are much smaller than the aggregates observed here. For example, fecal pellets falling at 100 m d^{-1} are typically 2-5×10^6 μm^3, equivalent to d = 200 μm (Small et al., 1979), compared to the mm sized aggregates dominating at A3. Thus, changes in zooplankton populations can be ruled out to explain the observed V_T increase at this time, although not through the entire season. Modelling the dynamics of the entire season would require integrating zooplankton activity.

4.3 Comparison with other studies

4.3.1 KEOPS 1

The comparison of our results with the size spectra obtained from UVP measurements at Station A3 during the early bloom (KEOPS2) and the late stage of the bloom (KEOPS 1) allows us to investigate the seasonal variability of particle production in the 0-200 m layer and the POC export flux (Fig. 11, Table 3). During summer (KEOPS1), the phytoplankton community was also dominated by *Chaetoceros* but shifted to *Eucampia antarctia* by the end of the bloom (Armand et al., 2008). Zooplankton abundance was 10-fold higher than during the early bloom and the community was dominated by copepods at copepodite stage (Carlotti et al., 2008). The mixed layer decreased from 150 m during early bloom to 70 m during summer. During KEOPS 2, V_T increased more than 20-fold from pre-bloom conditions, probably as a result of the higher diatom biomass (Armand., Pers. Com.), and coagulation as described in section 4.1. The value of V_T achieved by the time of the bloom decline in February (KEOPS1) was quite similar to that measured during early bloom for KEOPS2 but the vertical structure was different, with two subsurface maxima during KEOPS1, the first one present at the base of the ML (70 m). The larger V_T measured in January was associated with an increase in the fraction of large particles (Fig. 11c).

Below 200 m depth, V_T was still 10 times higher during the peak bloom as compared to early bloom. This resulted in 40- (at 200 m) and 10-fold (at 400 m) higher carbon export fluxes during the peak bloom than the early bloom (Table 3). During the decline of the bloom, V_T and POC flux were still higher than during early bloom. This is consistent with the general scheme of low production - high export at the end of the bloom put forward by Wassmann (1998). Our results provide insights on particle production and size distributions at different stages of the seasonal bloom. The early bloom occurs before zooplankton grazing dominates. This leads to a large increase in diatom abundance resulting in rapid aggregate formation and export from the surface ML. Later in the season, export becomes controlled by zooplankton grazing and fecal pellet production, as found from the gel trap analysis (Ebersbach and Trull, 2008). Despite the importance of zooplankton grazing in the late season, the presence of V_T maxima at the base of the ML indicates that coagulation still occurred during summer. An increase of aggregate formation through coagulation as result of high cell numbers in the ML and their disappearance due to grazing between the base of the mixed layer and 200 m traps could also explain the dominance of fecal aggregates in the gel traps during the summer

deployments. Combining KEOPS cruises to describe temporal scales of particle production and export (transient versus seasonal) is useful as a first step, but our limited observations highlight the need for high frequency data collection over long periods.

4.3.2 Potential impact of coagulation after iron fertilization

Our results can be compared to those from other iron fertilization experiments to understand the relative roles of coagulation and zooplankton grazing on particle export during different parts of the bloom cycle. However, it must be remembered that fertilization experiments differ in important aspects, including location, physical and chemical regimes, and observational techniques applied to determine stocks and fluxes. In addition, conclusions about carbon export from the surface often depend on sediment traps that are usually located well below the euphotic zone or surface ML, sampling events that have been filtered by intervening processes and offset by transit times. With this preamble, we compare our results to those from other iron fertilization studies by classifying them into those with phytodetritus export driven by diatoms and the rest, including those with a zooplankton-mediated export.

The artificial iron fertilization experiment SOIREE (February 1999) found an increase in phytoplankton biomass (Chl *a* = 2 mg m^{-3}) as a result of the iron addition, but no rapid removal of phytoplankton production. The export flux was low and driven by phyto-detrital aggregates (Waite and Nodder, 2001). Jackson et al. (2005) argued that the final abundance of phytoplankton cells was too low for rapid coagulation and sinking. There was a change in diatom settling rate associated with a change in iron status. The persistence of the bloom after iron was depleted implies that zooplankton grazing was not removing the particulate material.

The EIFEX (February–March 2004) environment was remarkably similar to that of KEOPS2 (Smetacek et al., 2012). The mixed layer was slightly shallower during EIFEX (100 m) than during KEOPS2 (150 m), but still relatively deep; the phytoplankton accumulation rates were also similar (0.03 to 0.11 d^{-1}). Iron fertilization stimulated a large diatom bloom that reached concentrations of about 2 mg Chl *a* m^{-3} four weeks after the fertilization started. There was little effect on vertical export during the first four weeks, but export then increased rapidly to 110–140 mmol C m^{-2} d^{-1}. This change was associated with mass mortality of several diatom species that formed rapidly sinking, mucilaginous aggregates of entangled cells and chains (Smetacek et al., 2012). This pattern of rapid formation of algal cells late in the bloom is similar to what we observed.

CROZEX investigated the impact of high biomass (Chl *a* = 2mg m^{-3}) associated with the bloom decline on carbon export during 2 legs (November 2004 and January 2005) (Venables et al., 2007). Carbon export fluxes estimated from a sediment trap in the highly productive naturally iron fertilized region of the sub-Antarctic waters were two to three times larger than the carbon fluxes from adjacent HNLC waters (Pollard et al., 2009). Vertical flux was dominated by a diverse range of diatoms, which suggests an important role for direct export, such as by coagulation.

In contrast, the particulate flux in the SAZ-Sense in a region of elevated biomass (Chl *a* = 1.9 mg m^{-3}) in the Sub Antarctic Zone east of Tasmania fuelled by enhanced iron was dominated by fecal aggregates (Ebersbach et al., 2011).

The LOHAFEX iron fertilization experiment was one of the few to use a particle measuring system for the water column, also the UVP (Martin et al., 2013). A cyclonic eddy low in silica on the Antarctic Polar Frontal Zone was fertilized with iron. In response, phytoplankton biomass almost doubled to 1-1.5mg Chl *a* m^{-3}, but 90% of it was in flagellates less than 10 μm instead of diatoms. There was no observable change in concentrations of particles larger than 100 μm or in vertical particle flux. There were several reasons proposed for the low export, including the lack of diatoms in the low silicate water and intense particle consumption, particularly at the base of the mixed layer (66 m).

5 Conclusions

It is clear that particle flux in the ocean is the result of many interacting processes, and none of these has been identified dominant across systems. In the present study, we were able to observe rapid aggregate formation and sedimentation of high concentrations of diatoms from the euphotic zone. Our observations are consistent with results from a one-dimensional model that includes only phytoplankton growth and coagulation. Our results demonstrate the utility of coagulation theory in understanding vertical flux and its importance to initiate the formation of large particles in the mixed layer and their subsequent transfer to depth during a bloom. Nevertheless, efforts are still required to measure large aggregates distribution at a high frequency to fill the temporal window between these short time events taking place during the early bloom and the possibly slower dynamics of summer. In addition, more effort is required to understand better vertical variations at a fine scale for all times and particularly

514 to estimate the transformative roles of microbes and zooplankton in decreasing the total
515 particle volume exported from the euphotic zone.

516 *Acknowledgements.* Thanks to the Kerguelen Ocean and Plateau Compared Study (KEOPS 2)
517 shipboard science team and the officers and crew of R/V *Marion Dufresne* for their efforts.
518 Christine Klaas provided helpful input on biological conditions. This research was supported
519 by the French Agency of National Research grant (# ANR-10-BLAN-0614). G. A. Jackson
520 was supported by US National Science Foundation (NSF) grant OCE09-27863. L. Stemmann
521 was supported by the chair VISION from CNRS/UPMC.

References

Alldredge, A. L. and Gotschalk, C.: In situ settling behavior of marine snow, Limnol. Oceanogr., 33, 339–351, 1988.

Armand, L. K., Cornet Barthaux, V., Mosseri, J., and Quéguiner, B.: Late summer diatom biomass and community structure on and around the naturally iron-fertilized Kerguelen Plateau in the Southern Ocean, Deep-Sea Res. II, 55, 653–676, 2008.

Assmy, P., Henjes, J., Klaas, C., and Smetacek, V.: Mechanism determining species dominance in a phytoplankton bloom induced by the iron fertilization experiment EisenEx in the Southern Ocean, Deep-Sea Res. I, 54, 340–362, 2007.

Blain, S. et al.: Effect of natural iron fertilization on carbon sequestration in the Southern Ocean, Nature, 446, 1070–1074, 2007.

Boyd, P. W. et al.: A mesoscale phytoplankton bloom in the polar Southern Ocean stimulated by iron fertilization, Nature, 407, 695–702, 2000.

Boyd, P. W. et al.: The decline and fate of an iron-induced subarctic phytoplankton bloom, Nature, 428, 549–553, 2004.

Buesseler, K. O., Andrews, J. E., Pike, S. M., and Charette, M. A.: The effects of iron fertilization on carbon sequestration in the Southern Ocean, Science, 304, 414–417, 2004.

Buesseler, K. O., Andrews, J. E., Pike, S. M., and Charrette, M. A.: Particle export during the Southern Ocean Iron Experiment (SOFeX), Limnol. Oceanogr., 50, 311–327, 2005.

Burd, A. B., Jackson, G. A., Particle aggregation, Annu. Rev. Mar. Sci., 1, 65–90, 2009.

Carlotti, F., Thibault-Botha, D., Nowaczyk, A., and Lefèvre, D.: Zooplankton community structure, biomass, and role in carbon fluxes during the second half of a phytoplankton bloom in the eastern sector of the Kerguelen Shelf (January–February 2005), Deep-Sea Res. II,

55, 720–733, 2008.

Carlotti, F., Harmelin, M., Nowaczik, A., Jouandet, M-P., Lefèvre, D.: Mesozooplankton structure and functioning during the onset of the Kerguelen Bloom during KEOPS2 survey, 2014.

549 Chever, F., Sarthou, G., Bucciarelli, E., Blain, S., and Bowie, A. R.: An iron budget during
550 the natural iron fertilisation experiment KEOPS (Kerguelen Islands, Southern Ocean),
551 Biogeosci., 7, 455–468, doi:10.5194/bg-7-455-2010, 2010.

552 Closset, I., Lasbleiz, M., Leblanc, K., Quéguiner, B., Cavagna, A-J., Elskens, M., Navez, J.,
553 and Cardinal, D.: Seasonal evolution of net and regenerated silica production around a natural
554 Fe-fertilized area in the Southern Ocean estimated from Si isotopic approaches, 2014.

555 De Baar, H. J. W., Boyd, P. W., Coale, K. H., Landry, M. R., Tsuda, A., Assmy, P., Bakker,
556 D. C. E., Bozec, Y., Barber, R. T., Brzezinski, M. A., Buesseler, K. O., Boye, M., Croot, P.
557 L., Gervais, F., Gorbunov, M. Y., Harrison, P. J., Hiscock,W. T., Laan, P., Lancelot, C., Law,
558 C. S., Levasseur, M., Maretti, A., Millero, F. J., Nishioka, J., Nojiri, Y., van Oijen, T.,
559 Riebesell, U., Rijkenberg, M. J. A., Saito, H., Takeda, S., Timmermans, K. R., Veldhuis, M. J.
560 W., Waite, A. M., Wong, C- H.: Synthesis of iron fertilization experiments: from the iron age
561 in the age of enlightenment, J. Geophys. Res., 110, 1–24, 2005.

562 Ebersbach, F. and Trull, T. W.: Sinking particle properties from polyacrylamide gels during
563 KEOPS: Controls on carbon export in an area of persistent natural iron inputs in the Southern
564 Ocean, Limnol. Oceanogr., 53, 212–224, doi:10.4319/lo.2008.53.1.0212, 2008.

565 Ebersbach, F., Trull, T. W., Davies, D., Moy, C., Bray, S. G., and Bloomfield, C.: Controls on
566 mesopelagic particle fluxes in the Sub-Antarctic and Polar Frontal Zones in the Southern
567 Ocean south of Australia in summer – perspectives from free-drifting sediment traps, Deep-
568 Sea Res. II, 58, 2260–2276, 2011.

569 Evans, G. T. and Parslow, J. S.: A model of annual plankton cycles, Biol. Oceanogr., 3, 327–
570 347, 1985.

571 Fasham, M. J. R., Ducklow, H. W., and McKelvie, S. M.: A nitrogen-based model of
572 plankton dynamics in the ocean mixed layer, J. Mar. Res., 48, 591–639, 1990.

573 Fasham, M. J. R., Flynn, K. J., Pondaven, P., Anderson, T. R., and Boyd, P. W.: Development
574 of a robust ecosystem model to predict the role for iron in biogeochemical cycles: a
575 comparison of results for iron-replete and iron-limited areas, and the SOIREE iron-
576 enrichment experiment, Deep-Sea Res., 53, 333–366, 2006.

577 Gelbard, F., Tambour, Y., and Seinfeld, J. H.: Sectional representations for simulating aerosol
578 dynamics, J. Colloid Interf. Sci., 76, 541–556, 1980.

579 Gervais, F., Riebesell, U., and Gorbunov, M. Y.: Changes in primary productivity and
580 chlorophyll *a* in response to iron fertilization in the southern Polar Frontal Zone, Limnol.
581 Oceanogr., 47, 1324–1335, 2002.

582 Guidi, L., Jackson, G., A., Stemmann, L., Miquet, J. C., Picheral, M., and Gorsky, G.:
583 Relationship between particle size distribution and flux in the mesopelagic zone, Deep-Sea
584 Res. I, 55, 1364–1374, doi:10.1016/j.dsr.2008.05.014, 2008.

585 Hoffmann, L. J., Peeken, I., Lochte, K., Assmy, P., and Veldhuis, M.: Different reactions of
586 Southern Ocean phytoplankton size classes to iron fertilization, Limnol. Oceanogr., 51, 1217–
587 1229, 2006.

588 Jackson, G. A.: Comparing observed changes in particle size spectra with those predicted
589 using coagulation theory, Deep-Sea Res. II, 42, 159–184, 1995.

590 Jackson, G. A.: Coagulation theory and models of oceanic plankton, in: Flocculation in
591 Natural and Engineered Environmental Systems, edited by: Droppo, I., Leppard, G., Liss, S.,
592 and Milligan, T., CRC Press, Boca Raton, FL, 271–292, 2005.

593 Jackson, G. A. and Kiørboe, T.: Maximum phytoplankton concentrations in the sea, Limnol.
594 Oceanogr., 53, 395–399, 2008.

595 Jackson, G. A. and Lochmann, S. E.: Effect of coagulation on nutrient and light limitation of
596 an algal bloom, Limnol. Oceanogr., 37, 77–89, 1992.

597 Jackson, G. A.,Waite, A. M., and Boyd, P.W.: Role of algal aggregation in vertical carbon
598 export during SOIREE and in other low biomass environments, Geophys. Res. Lett., 32,
599 L13607, doi:10.1029/2005GL023180, 2005.

600 Jassby, A. and Platt, T.: Mathematical formulation of the relationship between photosynthesis
601 and light for phytoplankton, Limnol. Oceanogr., 21, 540–547, 1976.

602 Jouandet, M. P., Blain, S., Metzl, N., Brunet, C., Trull, T. W., and Obernosterer, I.: A
603 seasonal carbon budget for a naturally iron-fertilized bloom over the Kerguelen Plateau in the
604 Southern Ocean, Deep-Sea Res. II, 55, 856–867, doi:10.1016/j.dsr2.2007.12.037, 2008.

605 Jouandet, M. P., Trull, T. W., Guidi, L., Picheral, M., Ebersbach; F., Stemmann, L., and
606 Blain, S.:Optical imaging of mesopelagic particles indicates deep carbon flux beneath a
607 natural ironfertilized bloom in the Southern Ocean, Limnol. Oceanogr., 5, 1130–1140, 2011.

608 Lampitt, R. S., Wishner, K. F., Turley, C. M., and Angel, M. V.: Marine snow studies in the
609 Northeast Atlantic Ocean: distribution, composition and role as a food source for migrating
610 plankton, Marine Biol., 116, 689–702, 1993.

611 Lasbleiz, M., Leblanc, K., Blain, S., Ras, J., Cornet-Barthaux, V., Helias Nunige, S.,
612 Queguiner, B.: Pigments, elemental composition (C,N,P,Si) and stoichiometry of particulate
613 matter, in the naturally iron fertilized region of Kerguelen in the Southern Ocean, 2014.

614 Laurenceau, E., Trull, T.W., Davies, D.M., Bray, S.G., Doran, J., Planchon, F., Carlotti, F.,
615 Jouandet, M-P., Cavagna, A-J., Waite, A.M., Blain, S. : Importance of ecosystem structure to
616 carbon export: insights from free-drifting trap deployments in naturally iron-fertilised waters
617 near the Kerguelen plateau, 2014.

618 Martin, P., Rutgers van der Loeff, M., Cassar, N., Vandromme, P., d'Ovidio, F., Stemmann,
619 L.,Rengarajan, R., Soares, M., González, H. E., Ebersbach, F., Lampitt, R. S., Sanders, R.,
620 Barnett, B. A., Smetacek, V., and Naqvi, S. W. A.: Iron fertilization enhanced net community
621 production but not downward particle flux during the Southern Ocean iron fertilization
622 experiment LOHAFEX, Global Biogeochem. Cy., 27, 1–11, doi:10.1002/gbc.20077, 2013.

623 Mongin, M., Moliant, M., and Trull, T. W.: Seasonality and scale of the Kerguelen plateau
624 phytoplankton bloom: A remote sensing and modeling analysis of the influence of natural
625 iron fertilization in the Southern Ocean. Deep-Sea Res. II, 55, 880-892, 2008.

626 Moore, J. K. and Abbott, M. R.: Surface chlorophyll concentrations in relation to the
627 Antarctic Polar Front: seasonal and spatial patterns from satellite observations, J. Marine
628 Syst., 37,69–86, 2002.

629 Park, Y. H., Fuda, J. L., Durand, I., and Naveira Garabato, A.C: Internal tides and vertical
630 mixing over the Kerguelen Plateau, Deep-Sea Res. II, 55, 583–593, 2008a.

631 Park, Y., Roquet, F., Fuda, J. L., and Durand, I.: Large scale circulation over and around the
632 Kerguelen Plateau, Deep-Sea Res. II, 55, 566–581, doi:10.1016/j.dsr2.2007.12.030, 2008b.

633 Picheral, M., Guidi, L., Stemmann, L., Karl, D. M., Iddaoud, G., and Gorsky G: The
634 Underwater Vision Profiler 5: An advanced instrument for high spatial resolution studies of
635 particle size spectra and zooplankton, Limnol. Oceanogr.-Meth., 8, 462–473,
636 doi:10.4319/lom.2010.8.462, 2010.

637 Planchon, F., Ballas, D., Cavagna, A-J., van der Merwe, P., Bowie, A.W., Trull, T.W.,
638 Laurenceau , E., Davis, D.M., and Dehairs, F.: Carbon export in the naturally iron-fertilized
639 Kerguelen area of the Southern Ocean using 234Th-based approach, 2014.

640 Pollard, R. T., Venables, H. J., Read, J. F., and Allen, J. T.: Large scale circulation around the
641 Crozet Plateau controls an annual phytoplankton bloom in the Crozet Basin, Deep-Sea Res. II,
642 54, 1905–1914, doi:10.1016/j.dsr2.2007.06.012, 2007.

643 Pollard, R. T. et al.: Southern Ocean deep-water carbon export enhanced by natural iron
644 fertilization, Nature, 457, 577–580, doi:10.1038/nature07716, 2009.

645 Salter, I., Lampitt, R. S., Sanders, S., Poulton, A. J., Kemp, A. E. S., Boorman, B., Saw, K.,
646 and Pearce, R.: Estimating carbon, silica and diatom export from a naturally fertilized
647 phytoplankton bloom in the Southern Ocean using PELAGRA: a novel drifting sediment trap,
648 Deep-Sea Res. II, 2233–2259, doi:10.1016/j.dsr2.2007.07.008, 2007.

649 Savoye, N., Trull, T.W., Jacquet, S., Navez, J., and Dehairs, F.: 234Th based export fluxes
650 during a natural iron fertilization experiment in the southern ocean (KEOPS), Deep-Sea Res.
651 II, 55, 841–855, doi:10.1016/j.dsr2.2007.12.036, 2008.

652 Small, L. F., Fowler, S. W., and Ümlü, M. U.: Sinking rates of natural copepod fecal pellets,
653 Mar. Biol., 51, 233–241, 1979.

654 Smetacek, V. et al.: Deep carbon export from a Southern Ocean iron-fertilized diatom bloom,
655 Nature, 287, 313–319, 2012.

656 Sommer, U.: Maximal growth rates of Antarctic phytoplankton: only weak dependence on
657 cell size, Limnol. Oceanogr., 34, 1109–1112, 1989.

658 Stemmann, L., Picheral, M., and Gorsky, G.: Diel variation in the vertical distribution of
659 particulate matter (> 0.15mm) in the NW Mediterranean Sea investigated with the
660 Underwater Video Profiler, Deep-Sea Res. I, 47, 505–31, 2000.

661 Timmermans, K. R., van der Wagt, B., and de Baar, H. J. W.: Growth rates, half-saturation
662 constants, and silicate, nitrate, and phosphate depletion in relation to iron availability of four
663 large, open-ocean diatoms from the Southern Ocean, Limnol. Oceanogr., 49, 2141–2151,
664 2004.

665 Tréguer, P. and LeCorre, P.: Manuel d'analyse des sels nutritifs dans l'eau de mer (Utilisation
666 de l'autoAnalyseur II), 2nd edn., Laboratoire d'Océanographie chimique, Univ. de Bretagne
667 Occidentale, 1975.

668 Turner, J. T.: Zooplankton fecal pellets, marine snow and sinking phytoplankton blooms,
669 Aquat. Microb. Ecol., 27, 57–102, 2002.

670 Tyrrell, T., Merico, A., Waniek, J. J., Wong, C. S., Metzl, N., and Whitney, F.: Effect of
671 seafloor depth on phytoplankton blooms in high-nitrate, low-chlorophyll (HNLC) regions, J.
672 Geophys. Res., 110, 1–12, 2005.

673 Uitz, J., Claustre, H., Morel, A., and Hooker, S. B.: Vertical distribution of phytoplankton
674 communities in open ocean: an assessment based on surface chlorophyll, J. Geophys. Res.-
675 Oceans, 111, 1–23, doi:10.1029/2005JC003207, 2006.

676 Venables, H. J., Pollard, R. T., and Popova, E. K.: Physical conditions controlling the
677 development of a regular phytoplankton bloom north of the Crozet Plateau, Southern Ocean,
678 Deep-Sea Res. II, 54, 1949–1965, doi:10.1016/j.dsr2.2007.06.014, 2007.

679 Waite, A. and Nodder, S. D.: The effect of in situ iron addition on the sinking rates and export
680 flux of Southern Ocean diatoms, Deep-Sea Res. II, 48, 2635–2654, 2001.

681 Wassmann, P.: Retention vs. export food chains: processes controlling sinking loss from
682 marine pelagic systems. Hydrobiologia, 363, 29–57, 1998.

683 **Tables**

684 Table 1: Date and time of the casts performed at Station A3.

685

Station	Date (dd-mm-yyyy)	Time (hh:mm)	Mixed layer depth (m)
A3-1	21-10-2011	2:20 AM	165
A3-2/1	15-11-2011	11:20 PM	143
A3-2/2	16-11-2011	7:50 AM	171
A3-2/3	″	11:30 AM	138
A3-2/4	″	7:15 PM	147
A3-2/5	17-11-2011	1:10 AM	123
A3-2/6	″	5:30 AM	163
A3-2/7	″	2:30 PM	124

686

687 Table 2: Symbols and parameter values used for the model. Conversion constants include:
688 Carbon to chlorophyll = 50 g C: g Chl *a*; carbon to nitrogen = 106 mol C:16 mol N.

689

Symbol	Quantity	Value	Units	Reference
d_c	Conserved diameter		cm	
d_a	Apparent diameter		cm	
d_1	Median algal diameter	20	μm	
D_{fr}	Fractal dimension	2	-	
G	Specific growth rate		d^{-1}	
G_{max}	Maximum specific growth rate	0.45	d^{-1}	Timmermans et al.
I	Irradiance		ly d^{-1}	
I_o	Surface irradiance		ly d^{-1}	Evans & Parslow
k	Total light attenuation=k_w+k_rP		m^{-1}	
k_r	Coefficient for light attenuation	0.03	m^2 (mmol	Fasham et al. 1990
k_w	Light attenuation of water	0.04	m^{-1}	Fasham et al. 1990
K_d	Half saturation constant	1	mmol N m^{-3}	Fasham et al. 2006
K_z	Eddy diffusivity	100	m^2 d^{-1}	Park et al. 2008a
m	Particle mass		g	
$n(d)$	Number spectrum for diameter		cm^{-4}	
$n(m)$	Number spectrum for mass m		cm^{-3} g^{-1}	
N	Nitrate concentration		mmol N m^{-3}	
Q_i	Particle mass in ith section		g	
r	Phytoplankton mortality rate	0.04	d^{-1}	Assmy et al. 2007
r_p	Relative light limitation		-	
r_n	Relative nitrate limitation		-	
v_i	Settling velocity for particle in		m d^{-1}	
V	Particle volume			
α_I	Slope of photosyn. curve		0.04 ly^{-1}	Evans & Parslow
α	Stickiness	1	-	Jackson et al. 2005
β	Coagulation kernels			
${}^1\beta_{i,j,l}$, ${}^2\beta_{i,i}$, ${}^3\beta_{i,i}$, ${}^1\beta_{i,i}$	Sectional coefficients			
ϕ	Phytoplankton concentration		mmol N m^{-3}	
λ_i	Disaggregation coef. for ith		d^{-1}	Jackson 1995
γ	Fluid shear	1	s^{-1}	Jackson et al. 2005
μ	Average algal growth rate		d^{-1}	

690

691 Table 3: Comparison of the POC fluxes (F_{POC} in mg m^{-2} d^{-1}) derived from particle size
692 distributions from the UVP, particle distributions from gel-filled sediment traps and sediment
693 trap PPS3/3 Technicap Inc, France (Laurenceau et al., this volume) during KEOPS2 and
694 KEOPS1 (Jouandet et al., 2011, Ebersbach et al., 2008).

		Winter KEOPS2	Spring KEOPS2	Mid summer KEOPS 1	End summer KEOPS1
F_{POC} at 200 m ($mg\ m^{-2}\ d^{-1}$)	$F=Ad^b$	1.75	23.11	869	58
	Gel trap		66		
	Trap PPS3		27 ± 8		
F_{POC} at 350 m ($mg\ m^{-2}\ d^{-1}$)	$F=Ad^b$	1.04	3.50	326	67

695

696

Figure captions

Figure 1: Vertical distribution of sigma (black line), fluorescence (green line) and turbidity (blue line) (A) and vertical profiles of total abundance (N_T) and total volume (V_T) at the first cast of A3, during winter (A3-1, 21 of October).

Figure 2: Temporal evolution of density (A), fluorescence (B) and turbidity (C) during the spring survey. The red line shows the mixed layer depth.

Figure 3: Vertical distribution of the concentration of NO_3 (A); Total Chl *a* (T_{chla}), and T_{chla} associated with micro-($Tchla_{micro}$), nano-($Tchla_{nano}$), and picophytoplankton ($Tchla_{pico}$) (B). The filled symbols indicate pre-bloom stage; the hollow symbols indicate early bloom stage.

Figure 4: Vertical distribution of N_T and V_T for the different casts during early bloom stage.

Figure 5: Difference of the size spectra abundance between the depth of the volume maxima (Z_{max}) and the euphotic layer (Z_e) (A) and cumulative volume distribution (B) in the euphotic layer (dashed line) and at the depth of the V_T sub surface maxima (solid line).

Figure 6: Volume distribution size spectra along vertical axis on the 17 of November at 1:10 AM (A3-2/5). The white line indicates values at 150 m, the bottom of the model regime.

Figure 7: Distribution of V_T below the surface mixed layer (A). Normalized particles size spectra abundance average over the 320-350 layer (dotted line) and 100-200 m layer (solid line) (B).

Figure 8: Scatter plots of fluorescence and V_T for the 3 layers: surface to base of ML (A), base of ML to 200 (B) and >200 m (C). Large symbols indicate the means for a profile in the panel depth range.

Figure 9: Model results for vertical distribution through time of phytoplankton (µg Chl L^{-1}) (A; phytoplankton concentration does not include any algae present in aggregates), nitrate (µM) (B), and V_{Ta} (ppm) (C). Contour interval is 0.1 µg Chl L^{-1}(A), 0.5 µM (B), 1 ppm (C). The calculation assumes that the UVP only measures aggregates larger than 100 µm.

Figure 10: Distribution of apparent particle volume, nVd_a, as a function of depth and d_a as calculated by the model at 20 d. Because the value of d_a is plotted on a logarithmic scale, the area under the curve for each depth is proportional to total particle volume V_{Ta}.

725 **Figure 11**: A, B: comparison of the total volume profiles measured during KEOPS2 in
726 October (A3-1, blue), November (A3-2/7, green), and during KEOPS1 in January (red) and
727 February (brown). The depth scale for B is expanded to cover only 200-500m. C, D:
728 comparison of the normalised size spectra in the 0-200 m (C) and 200-400 m layer (D). The
729 colours indicate profiles as in A, B.

730 Figure 1

731

732

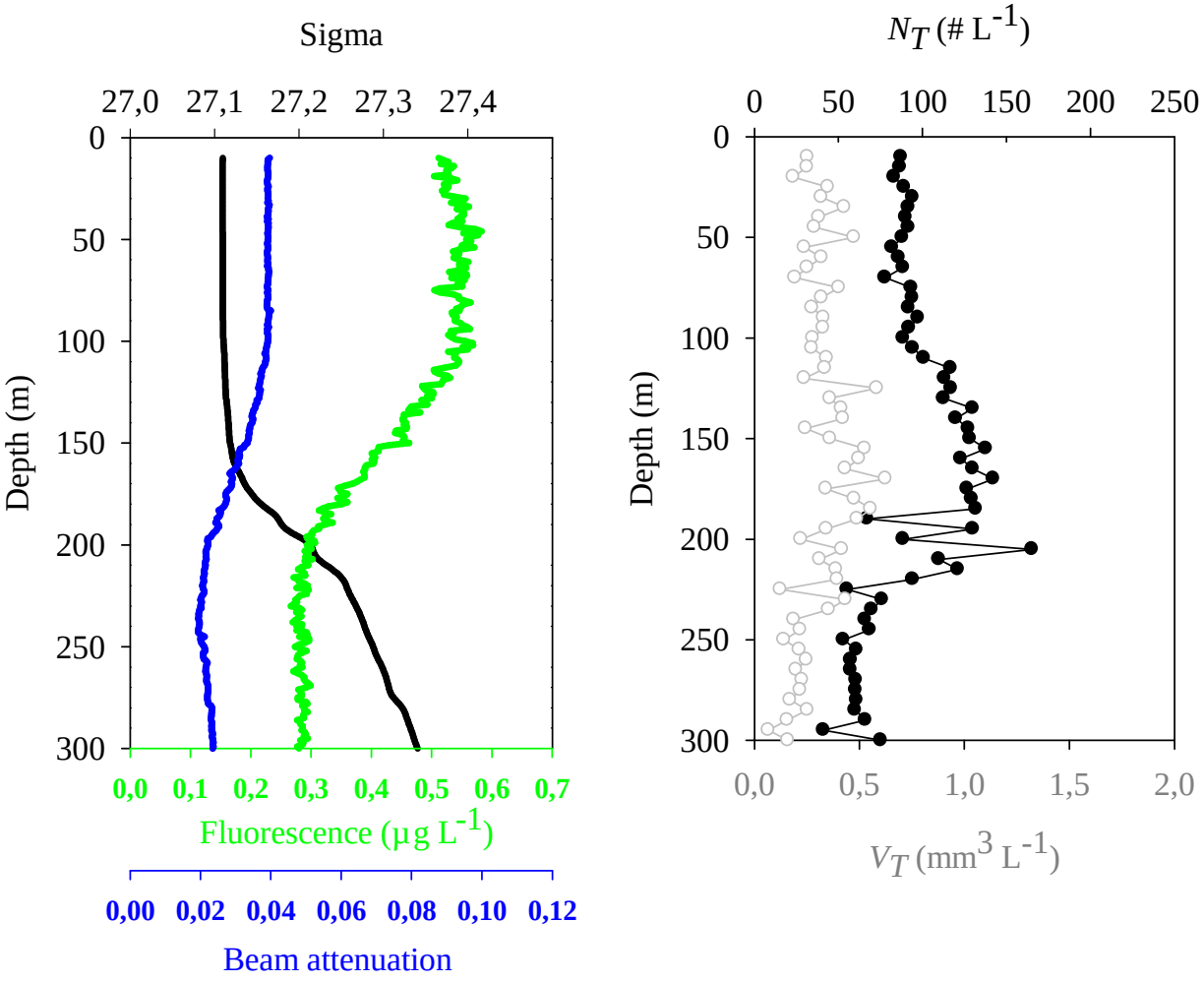

733

734

735

736

737

738

739

740 Figure 2

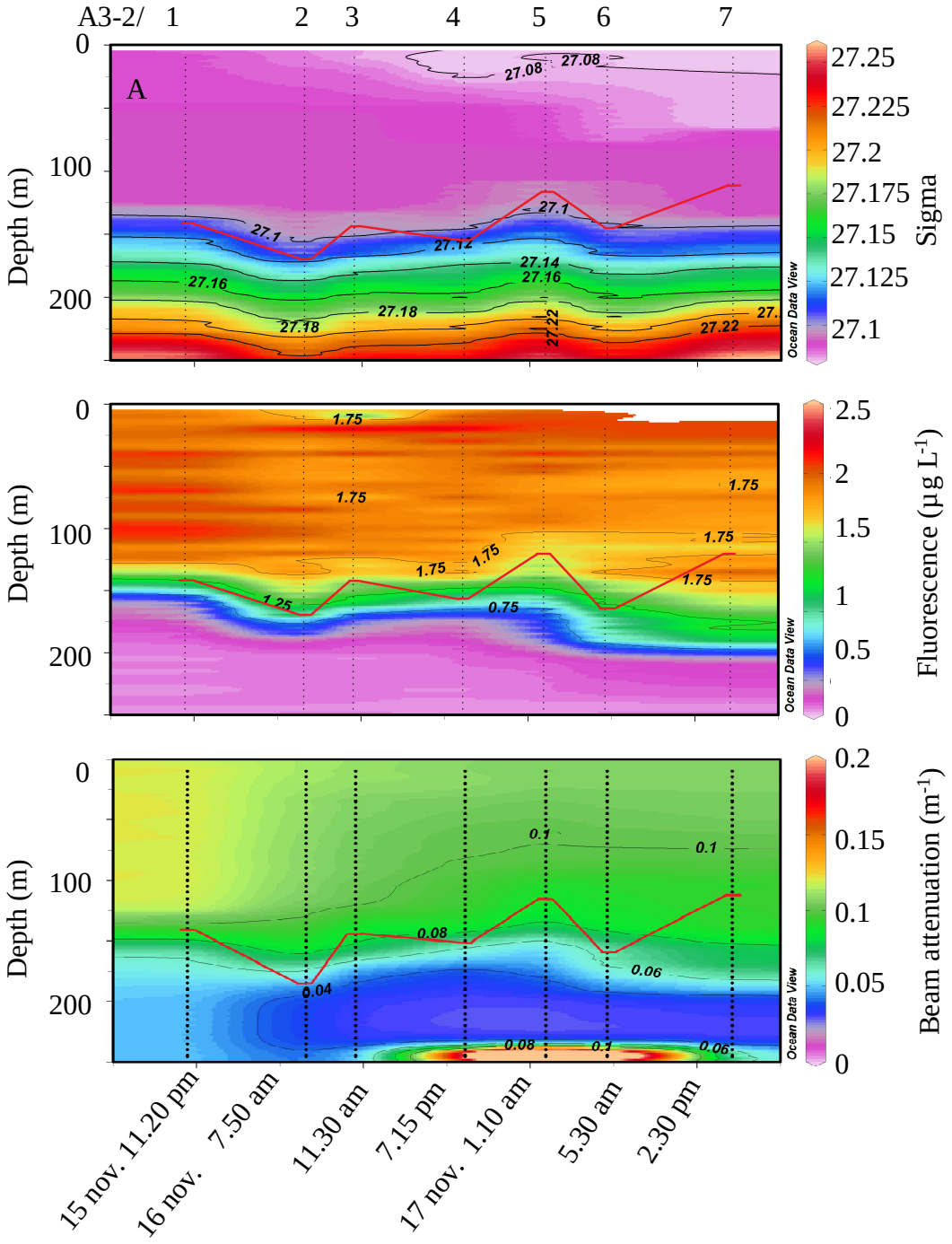

741

742 Figure 3

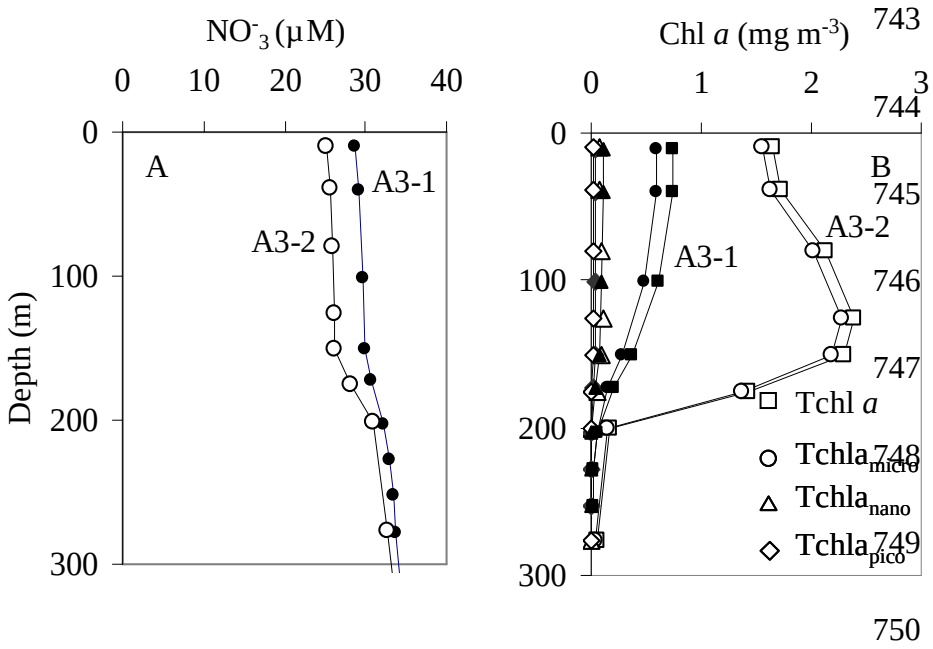

751

752 Figure 4

753

754

755

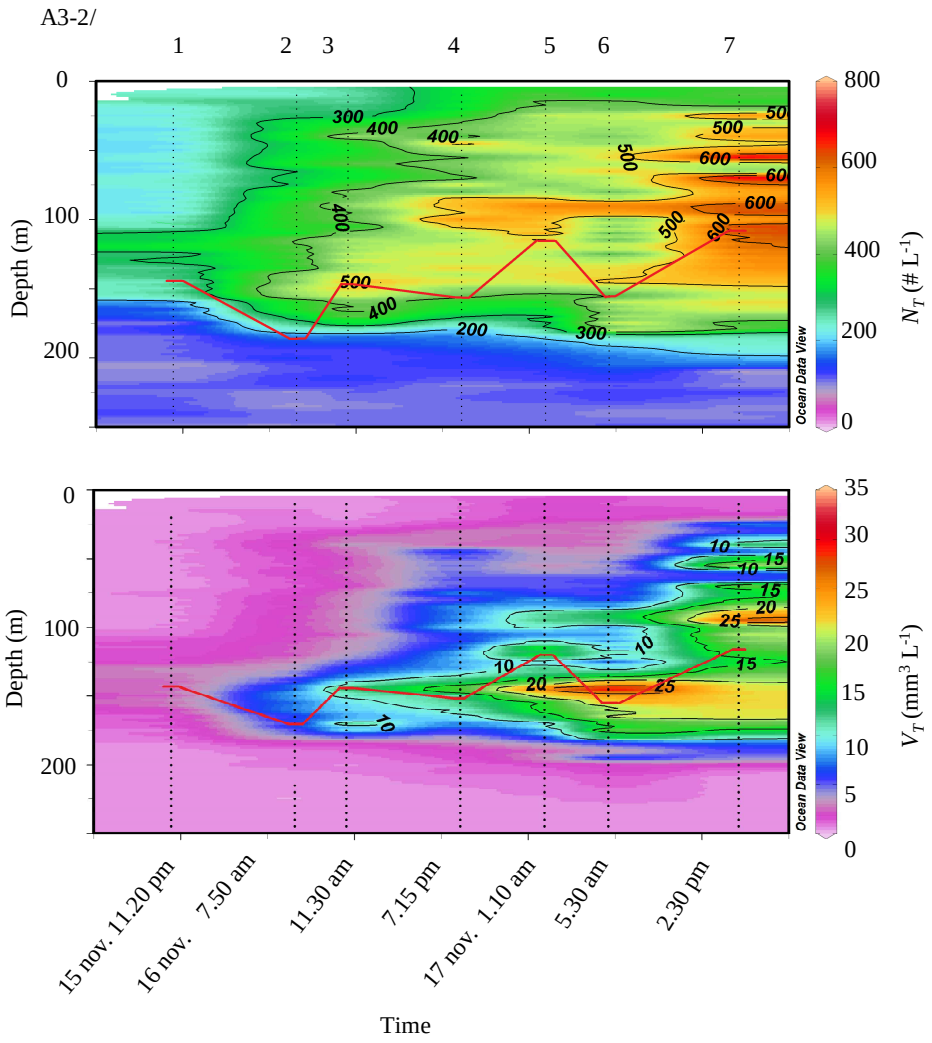

Figure 5

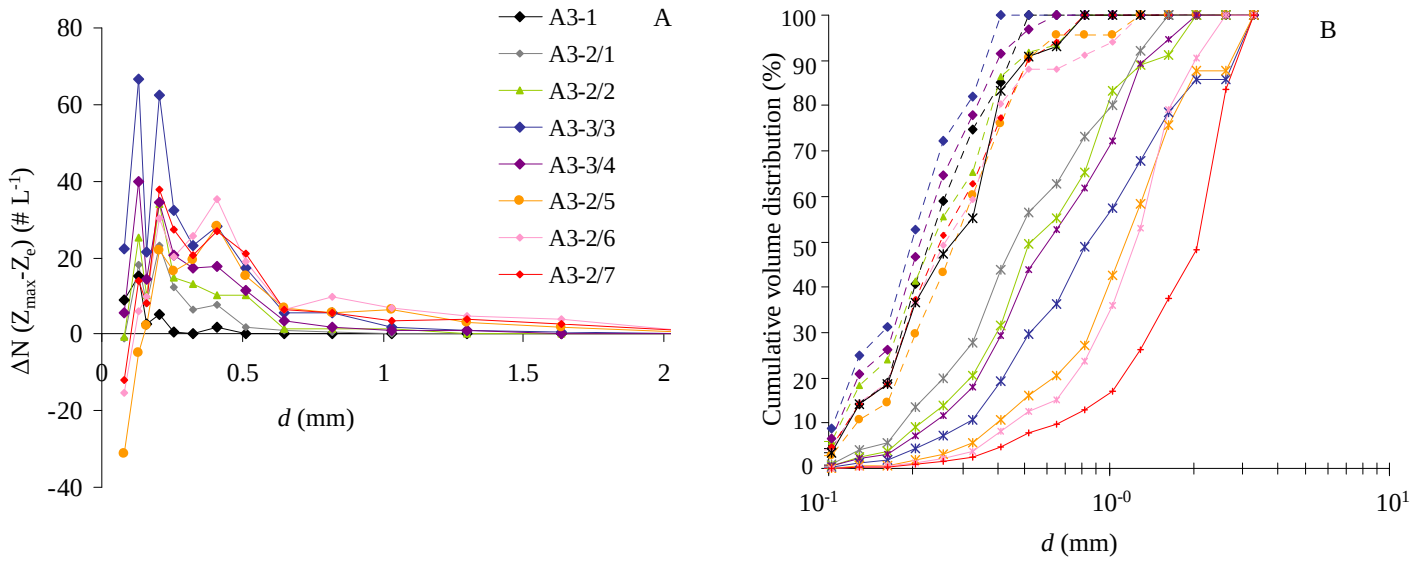
A
A3-1
A3-2/1
A3-2/2
A3-3/3
A3-3/4
A3-2/5
A3-2/6
A3-2/7
ΔN (Z_max-Z_e) (# L^-1)
d (mm)
B
Cumulative volume distribution (%)
d (mm)

765 Figure 6

766

767

768

769

770

771

772

773

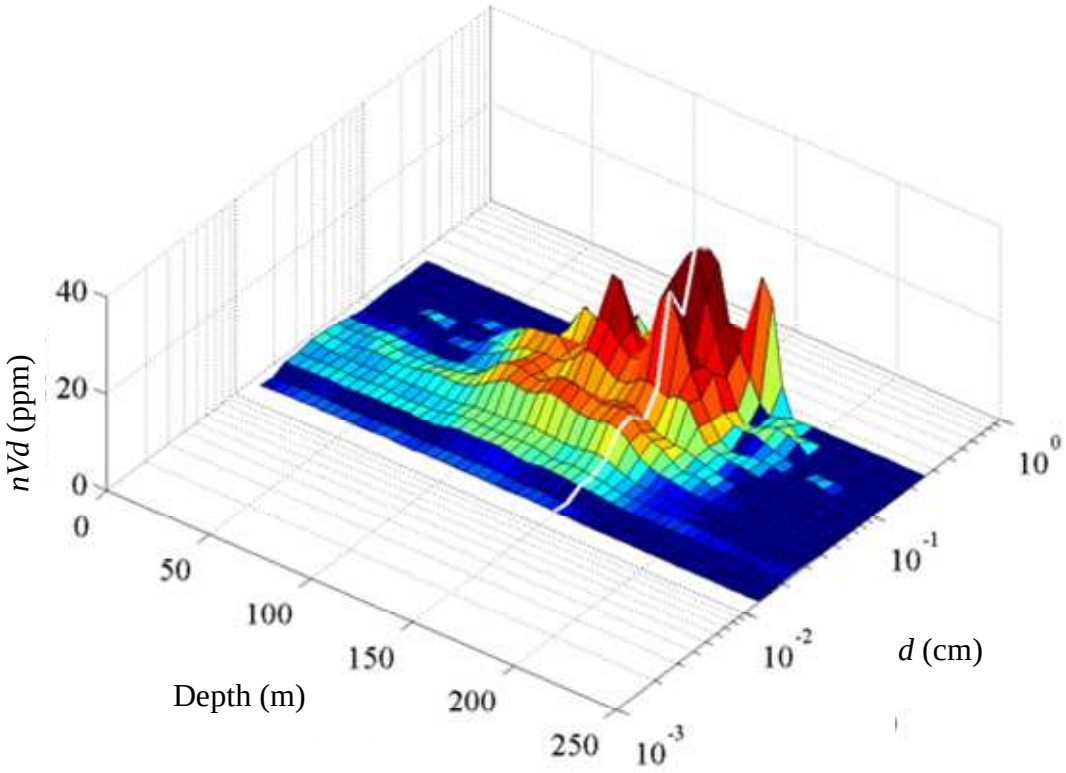

Figure 7

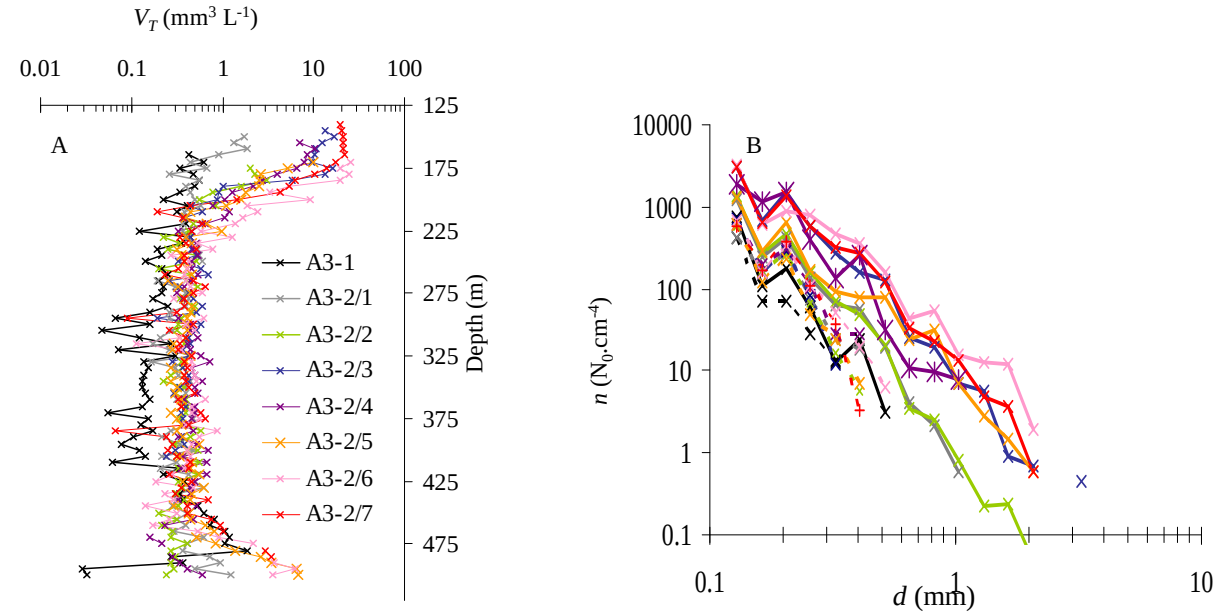
V_T (mm^3 L^{-1})
0.01
0.1
1
10
100
A
125
175
225
275
325
375
425
475
Depth (m)
A3-1
A3-2/1
A3-2/2
A3-2/3
A3-2/4
A3-2/5
A3-2/6
A3-2/7
B
10000
1000
100
10
1
0.1
n (N$_0$,cm^{-4})
0.1
1
10
d (mm)

Figure 8

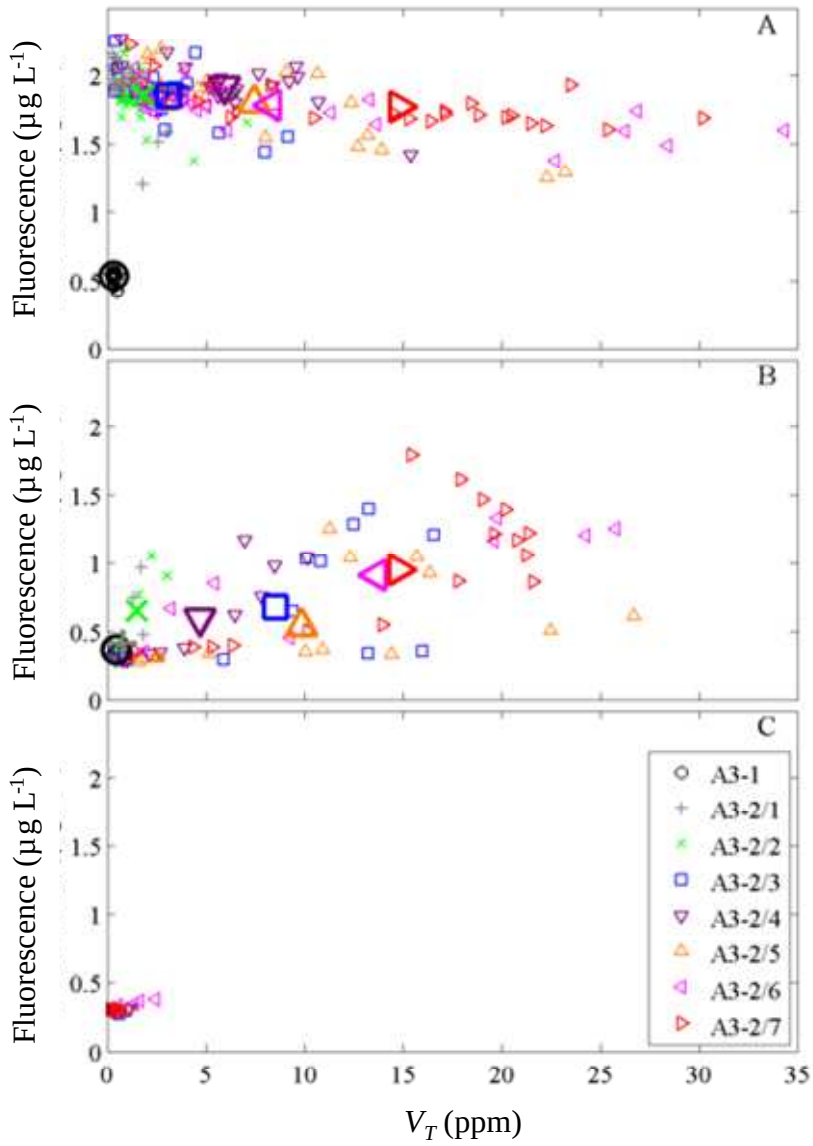
A
B
C
Fluorescence (µg L-1)
Fluorescence (µg L-1)
Fluorescence (µg L-1)
0
0.5
1
1.5
2
0
5
10
15
20
25
30
35
VT (ppm)
A3-1
A3-2/1
A3-2/2
A3-2/3
A3-2/4
A3-2/5
A3-2/6
A3-2/7

Figure 9

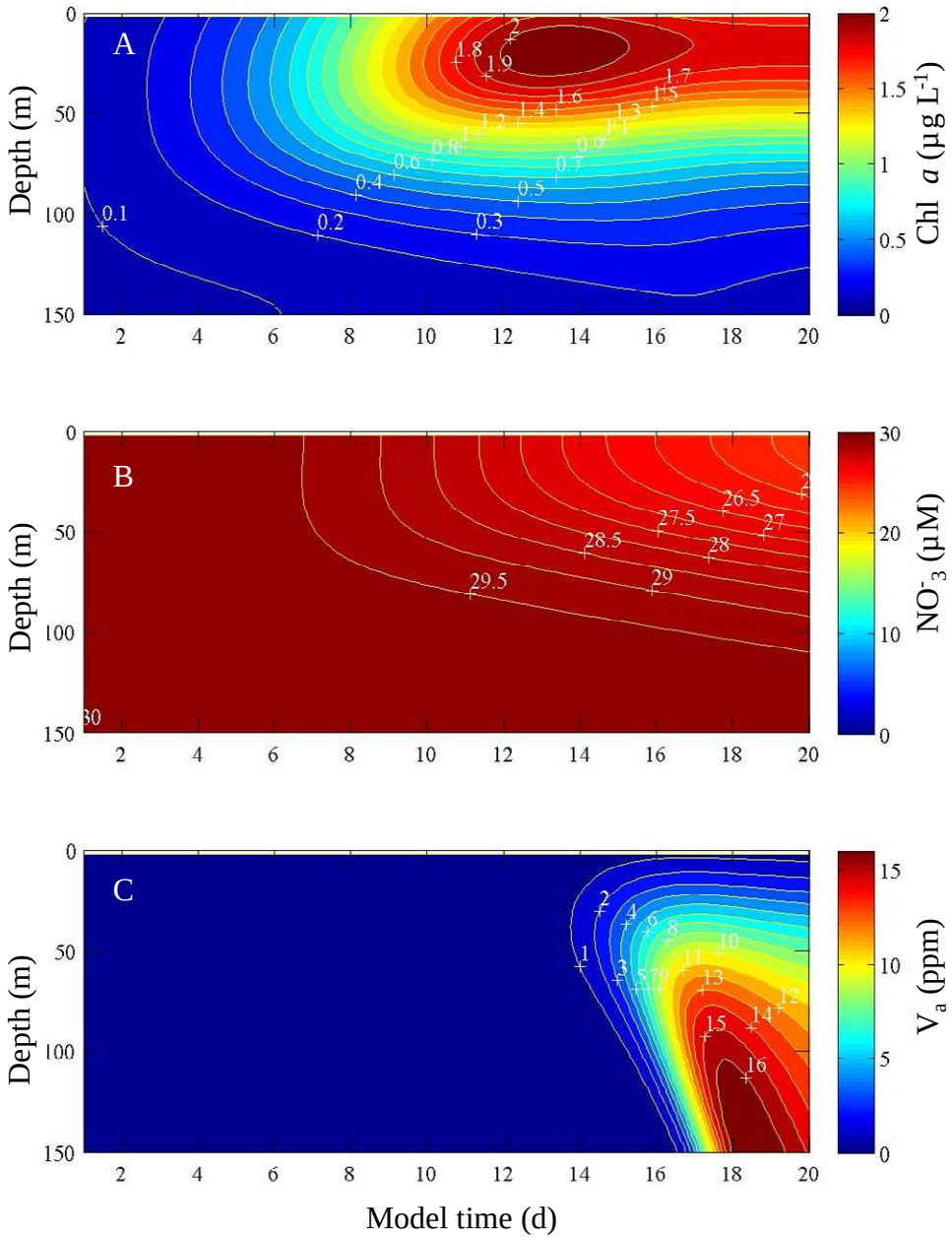

821 Figure 10

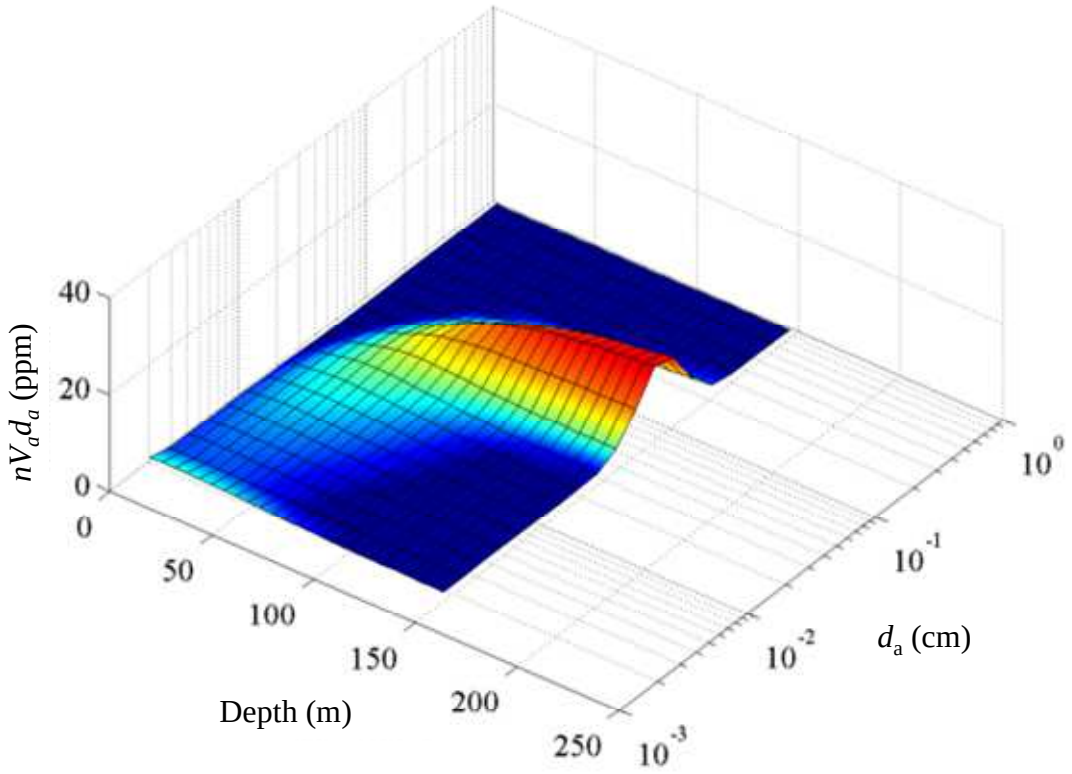

822

823 Figure 11

824

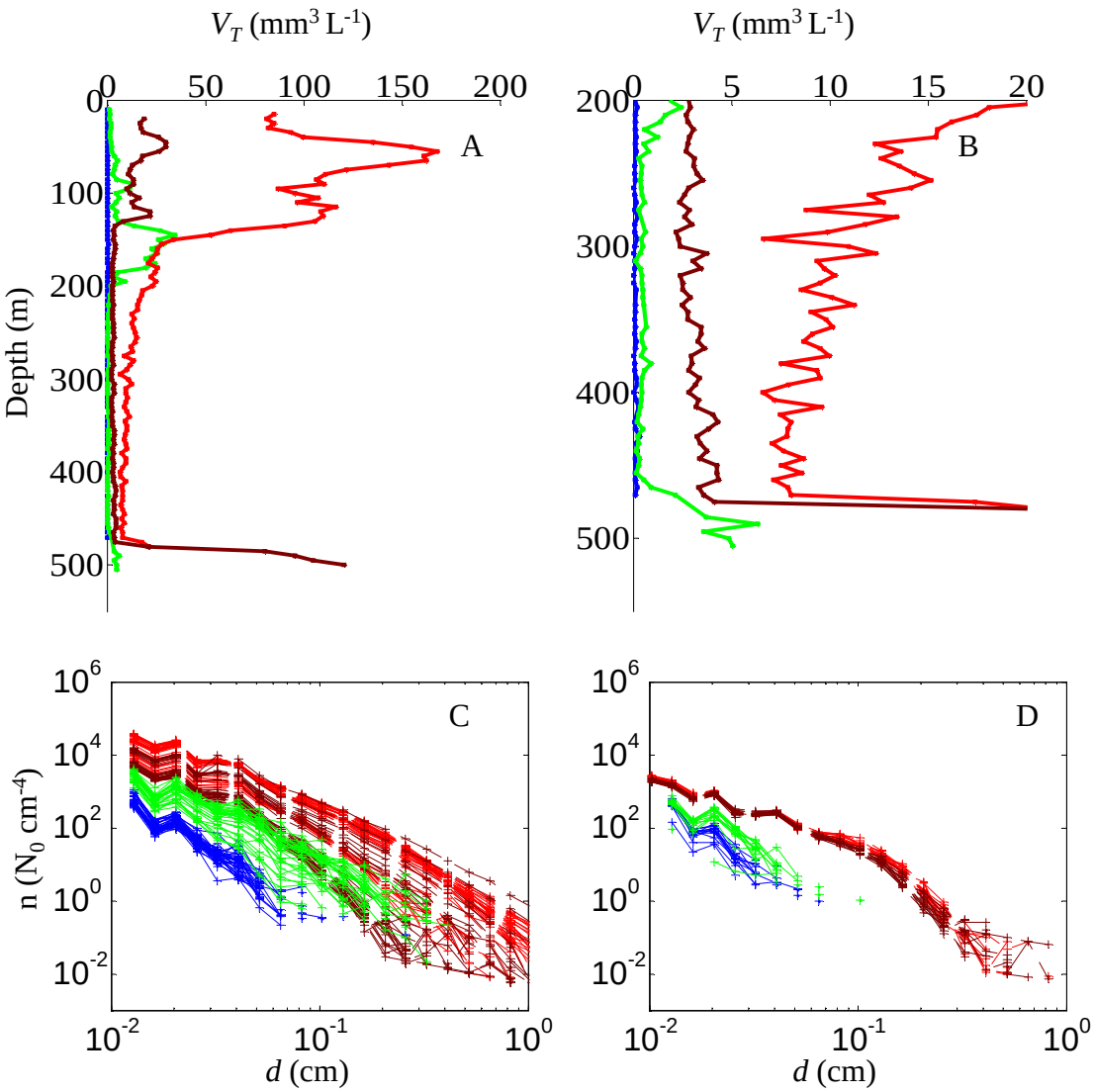

825